Advanced Research Design

Hydrodynamic modelling of a sea-crossing bridge in Maldives

Open Access

Hassan Shiraz[1],[*], M. H. Jamal[1]

[1] Department of Engineering at Faculty of Engineering Science and Technology (FEST), The Maldives National University, Rahdhebai Higun, Machangolhi Male', 20371, Maldives

ARTICLE INFO	ABSTRACT
	'Gaadhoo Koa Channel' is an atoll pass located in the southern tip of Malé Atoll, Maldives, separating the capital city, Malé, and the main international airport, Hulhulé island. The Gaadhoo Koa channel is known for its strong tidal flow and strong swell waves and is located in a strategic area which includes the main shipping lane for Malé port and also marine traffic lanes connecting both Malé and Hulhulé with nearby islands. Recently, a sea-crossing bridge has been constructed across the channel connecting these two islands. This involved in the construction of 21 bridge piers across the channel which raised concerns on the potential negative impacts on the flow regime in the vicinity of the bridge. This paper presents a numerical modelling study to investigate the hydrodynamic impact of the bridge piers in the Gaadhoo Koa channel using Delft3D-FLOW modelling software. The model results were calibrated against water level data from Hulhulé station and finally model simulations were run to assess the hydrodynamic impact of the bridge piers. The results indicated that the flows in the close vicinity of the bridge were reduced with the introduction of bridge piers. Also, the magnitude of flow velocity reduced around bridge piers and increased in between bridge piers. Furthermore, the overall velocity distribution in the northern region from the bridge showed a decreasing pattern while the southern region showed an increasing pattern: peak velocity in the northern region decreased by 7.3 % at about 500 m from bridge whereas peak velocity in the southern region raised by 33% at also about 500 m from bridge. Based on these findings, it can be considered that the introduction of bridge piers can have a considerable impact on the hydrodynamic conditions of Gaadhoo Koa atoll pass.
Keywords: Gaadhoo Koa atoll pass; sea-crossing bridge; bridge piers; numerical modelling; Delft3D-FLOW	

1. Introduction

The Gaadhoo Koa atoll pass seperating Hulhulé and Malé Island in the Maldives is the main shipping lane for Malé port. The channel experiences strong tidal flow and receives strong swells from the southeast (SE) direction. In particular, the wave conditions on the SE reef corner of Malé, which is a prominent surf spot, and on the southern tip of Hulhulé Island are particularly strong. A

---

[*] Corresponding author.
E-mail address: hassan.shiraz@mnu.edu.mv (Hassan Shiraz)

water crossing bridge connecting these two islands has been constructed and opened in August 2018, covering an overwater length of 1.39 km [3]. Some studies [7] has shown that the hydrodynamics of overwater bridges has caused notable changes in the flow fields over a domain that can extend as far as one km from bridge locations. These changes were most prominent in the vicinity of bridge piers. However, there is limited literature on the effect of overwater bridges in atoll environments. Hence, it is essential to predict potential hydrodynamic changes in order to assess the physical impact of the overwater bridge on the flow field across Gaadhoo Koa channel. Therefore, the objectives of this work were to develop a numerical model to simulate the hydrodynamics of Gaadhoo Koa region and to assess the hydrodynamic impact of sea-crossing bridge across the channel.

In this study, a two-dimensional hydrodynamic model was setup for the Gaadhoo Koa region which comprises gentle reef slopes on either side of a deep oceanic channel. Only the flow module of the model programme, which focuses on unsteady flows due to tidal and meteorological forces was considered in this study. Model was calibrated using the observed water level data from Hulhulé station. After that, simulations were run with the effect of bridge piers included and the impact on hydrodynamic conditions in relation to current and tidal flows across the channel were evaluated.

2. Literature review
2.1 Hydrodynamics of the Site

The Gaadhoo Koa atoll pass between Malé and Hulhulé Island has a channel width of 1400 m. The channel area experiences strong tidal currents and receive strong swells from the southeast direction accompanied by strong winds.

Based on the gauge data collected from sea level monitoring station in Hulhulé, it has been reported that the tides along the east coast of Malé is in the category, 'Mixed Semidiurnal' with two high tides and two low tides per day of varying amplitudes [8]. The spring tidal range and the neap tidal range were 0.652m and 0.176 respectively and the monthly mean sea level ranged between 8-15 cm. The maximum mean sea level change was recorded between December and January while the minimum level was recorded during September to October. Besides the monthly variability of tidal water levels, past records show a significant inter annual variability in the sea level. The long-term annual sea level data for the past 20 years indicates a rise of 3.753 mm per year in Malé [12].

The waves observed along the Maldives islands can be classified into two major types. The first type is the monsoon driven wind waves with a period of 3 to 8 seconds and the second type is ocean swells generated by distant storms with a period ranging from 8 to 20 seconds [9]. These waves are typically strongest during April – July in the southwest (SW) monsoon period. The satellite altimetry wave climate data for the region indicates the dominant swell waves approach from the southwest to southerly directions [17] with a peak significant wave height of 1.8 m in June. It has also been reported that the region has observed swells generated north of the equator with heights of 2 to 3 m [12]. The bridge site is located on the SE rim of the atoll rim and is fairly protected from the northeast (NE) swells while being well exposed to swell waves approaching from SE direction. Hence it is expected that the site is more susceptible towards wave action during the SW monsoon and transition period.

Currents that affect the reef pass can be caused by the interaction of oceanic currents, tidal currents, local wind-induced currents and wave-induced currents. Some studies indicate that ocean currents and tidal currents to be the dominant forms in the region [4]. Ocean surface currents are driven by the wind action [15] and the current regime in the Indian Ocean is greatly influenced by the monsoon climate. In the Maldives archipelago the currents flow westward during the NE monsoon

period, and they flow eastward during the SW monsoon period [12]. Tidal currents are strongest during spring tide periods when the tide range is greatest [4].

2.2 Hydrodynamic Impacts of Sea-Crossing Bridges

The literature on the numerical modelling studies on hydrodynamical impacts associated with water crossing bridges is limited. Guo *et al.*, [7] simulated the changes in the tidal flow field in Quanzhou Bay due to a newly constructed sea crossing bridge. The results showed that slow flow areas were present in front of bridge piers due to the influence of rising and falling tides. Furthermore, slow flow areas were also formed at the back of the piers after the rising and falling tides passed the piers. The upstream and downstream flow along the bridge was found to be influenced over a distance approximately 1 km away. It was also found that sediment deposits around the main bridge pier increased while the sediment suspension decreased in between piers. These changes could potentially impact the navigation in the Quanzhou Bay. Similarly, Pun and Law [14] studied the influence of the bridge piers of six bridges on the tidal exchange in Rambler Channel located in Hong Kong. It was observed that the combined effect of all the bridges significantly decreased the tidal flow rate, restricting the tidal movement in the channel. Additionally, it was noted that the bridge piers modified the tidal flow path at the surface water layer, triggering a negative impact to flushing out contaminants from the channel. Li *et al.*, [10] also simulated the hydrodynamic processes due to a water-crossing bridge in Jiaozhou Bay, China, and found that the bridge significantly affected the hydrodynamics at the bay entrance, waterways and north side of the bridge.

Most of the studies show that the influence zone of hydrodynamic impact due to bridges were mainly limited to the regions in the close vicinity of the bridge. For instance, the hydrodynamic modelling of the Hangzhou Bay Bridge [13] indicated that the impact of bridge piers on the hydrodynamic setting was limited to a small region surrounding the bridge. This suggests that the relative size of the bridge span and surrounding water area could affect the degree of the impact. On the other hand, the impact of flow changes due to piers will be much greater if the bridge lies in a channel subjected to strong current and complex terrain [18].

3. Methodology

Figure 1 displays a flow chart of the methodologies that were used in this study. The flowchart comprises four main phases: (1) model selection (2) model inputs (3) model setup and (4) model simulation and analysis. Each phase is detailed in the following sections.
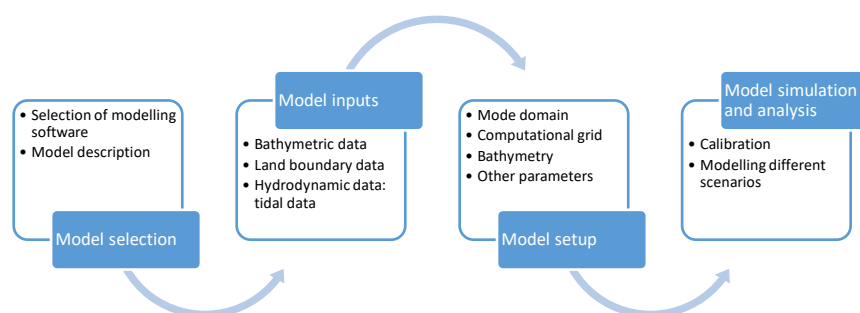
Fig. 1. *Flowchart of the study*

3.1 Model selection

There are a broad range of numerical modelling software available for hydrodynamic modelling including Telemac-2D model, MIKE21 model and Delft3D. A background study of these three software was conducted to determine the best modelling option. The main constraints considered in software selection were their costs (if any) and availability of documentation. MIKE21 was not possible as it was an expensive software to acquire. On the other hand, Telemac-2D and Delft3D are freely available as open source software. Eventually it was decided to use Delft3D because there are more documentations and a more active user community when compared to Telemac2D.

The Delft3D is a multi-disciplinary software suite developed to model unsteady water flow, temperature, salinity and cohesive/non-cohesive sediment transport in shallows seas, estuarine and coastal areas, rivers and lakes. The Delft3D-FLOW module was used to model water motion due to tidal and meteorological forcing by solving the unsteady shallow-water equations that consist of the continuity equation, the horizontal momentum equations, and the transport equation under the shallow water and Boussinesq assumptions by an implicit finite difference method on an unstructured grid. The continuity equation and momentum equations can be described as follows [5]

$$\frac{\partial h}{\partial t} + \frac{\partial Uh}{\partial x} + \frac{\partial Vh}{\partial y} = \int_0^h (q_{in} - q_{out})dz + P - E = Q \tag{1}$$

with U and V, the depth averaged velocities. Q represent the contributions per unit area due to the discharge or withdrawal of water, precipitation and evaporation with q_{in} and q_{out} the local sources and sinks of water per unit of volume respectively, P the non-local source term of precipitation and E non-local sink term due to evaporation. The momentum equations in x- and y-direction are given by

$$\frac{\partial u}{\partial t} + u\frac{\partial u}{\partial x} + v\frac{\partial u}{\partial y} + w\frac{\partial u}{\partial z} - fv = -\frac{1}{\rho_0}\frac{\partial P}{\partial x} + F_x + \frac{\partial}{\partial z}\left(v_V\frac{\partial u}{\partial z}\right) + M_x \tag{2}$$

$$\frac{\partial v}{\partial t} + u\frac{\partial v}{\partial x} + v\frac{\partial v}{\partial y} + w\frac{\partial v}{\partial z} - fu = -\frac{1}{\rho_0}\frac{\partial P}{\partial y} + F_y + \frac{\partial}{\partial z}\left(v_V\frac{\partial v}{\partial z}\right) + M_y \tag{3}$$

where v_V is the vertical eddy viscosity coefficient. Density variations are neglected, except in the baroclinic pressure terms, $\partial P/\partial x$ and $\partial P/\partial y$ represent the pressure gradients. The forces F_x and F_y in the momentum equations represent the unbalance of horizontal Reynolds stresses. M_x and M_y represent the contributions due to external sources or sinks of momentum.

3.2 Model Inputs

Bathymetric data was obtained from 'The General Bathymetric Chart of the Oceans' [2] and tide data measured from tide gauge located in Malé International Airport was obtained from University of Hawaii Sea Level database [1].

3.3 Model Domain

The model domain (Figure 2) was chosen in such a way that it represented the bridge site and all the islands connected by the bridge. The domain extends 7 km horizontally and 10 km vertically encompassing the two islands, Malé and Hulhulé, connected by a water-crossing bridge. This was

used as a basis to create the land boundary input file for Delft3D-FLOW GUI.
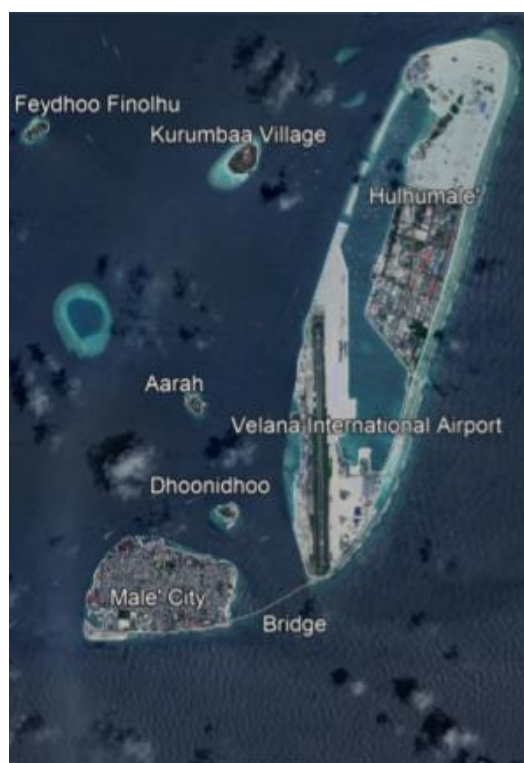
Fig. 2. Model area showing bridge location, atoll pass and the surrounding islands

3.4 Computational Grid

For this work, a rectilinear computational grid was generated using the Delft3D RGFGRID tool. In order to save computation time, the resolution of grid was refined in such a way that the areas lying outside the hypothesised influence zone due to the bridge had a lower resolution compared to the vicinity of the bridge. The resulting computational grid had 134 cells in the M (horizontal)-direction and 182 cells in the N (vertical) -direction with a total of 20,483 grid cells. For a good quality grid, the orthogonality should be less than 0.02, aspect ratio must be in the range [1 to 2] and M/N smoothness should be less than 1.2 with a maximum value of 1.4 in the areas of interest [5]. Using the tools in RGFGRID tool, it was found that all of these conditions were satisfied. The final computational grid is presented in Figure 3.

3.5 Bathymetry

The bathymetric data was automatically generated in terms of cartesian coordinates using the Delft3D Dashboard too which is based on 'The General Bathymetric Chart of the Oceans' [2]. Although the resolution of this data was low, this was the only data available at the time of model setup. Hence, some post processing of the generated data was carried out using the QUICKIN tool which allowed to copy depths into samples and interpolate the resulting samples by triangular interpolation to obtain depth at each grid cell of the generated grid. The final bathymetry for the model domain is presented in Figure 4.
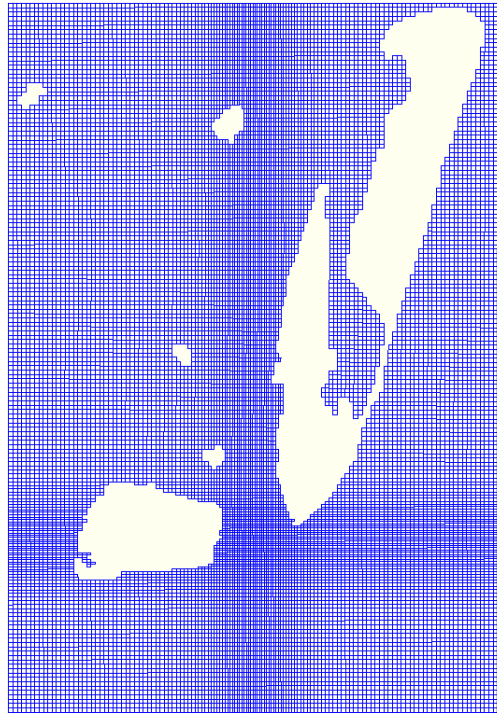
Fig. 3. Generated computational grid in RGFGRID window
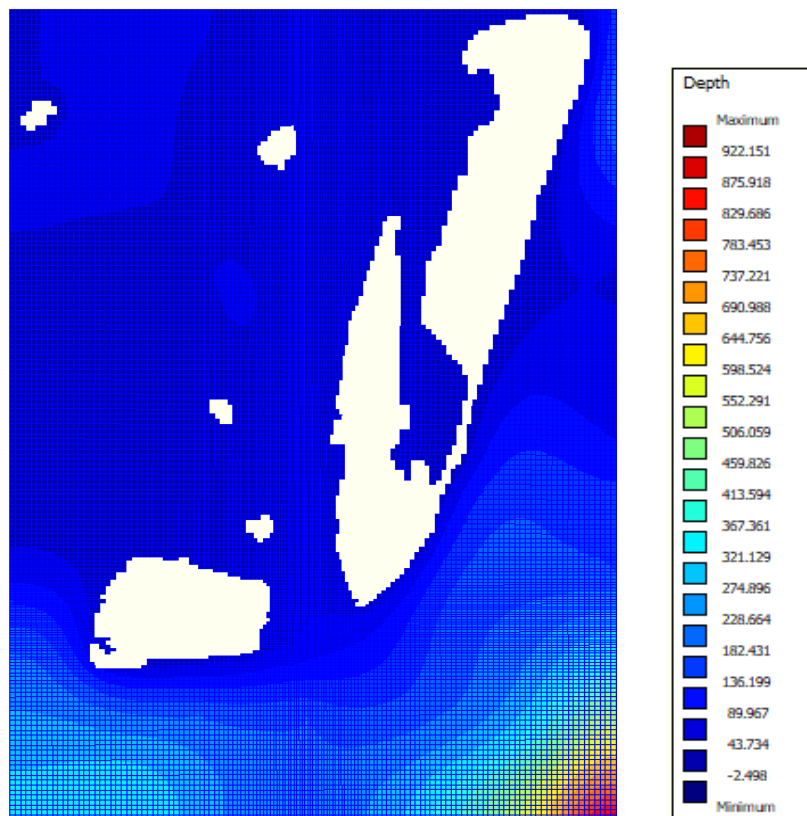
Fig. 4. Top view of the bathymetry layout in QUICKIN window

3.6 Boundary conditions

Boundary conditions in the form of astronomical constituents at all the four open boundaries surrounding the model domain were generated from the Delft Dashboard tool using tidal constituents from the Oregon State University global inverse tide model containing 13 tidal constituents [6].

3.7 Time-step

In order to maintain the numerical stability and accuracy of the model in Delft3D-Flow, the values of courant number were checked. The courant number, C, is given by

$$C = 2\Delta t\sqrt{gH}\sqrt{\frac{1}{\Delta x^2} + \frac{1}{\Delta y^2}} \qquad (4)$$

where Δt is the time step, g is the acceleration of gravity, H is the total water depth and Δx and Δy are the smallest grid spaces in M and N-direction of the mode domain. Generally, the courant number should not exceed a value of ten [5]. The Courant number of the model domain was evaluated using the QUICKIN and a step time of 1.5 seconds was adopted as this was the minimum time for which courant number was less than ten.

3.8 Model Calibration

During the calibration stage, the main focus was to calibrate the water levels and also the current velocity. However, due to unavailability of observed current data, only water level calibration was considered. Water level observations over a period of thirty days from Hulhulé tide station was used for calibration against modelled results for both spring and neap tide conditions. The model performance was then assed based on minimum level of performance indicators in coastal hydrodynamic models defined in terms of Root Mean Square Error ($RMSE$), Bias, Correlation (R) and Scatter Index (SI) [16]. These performance indicators are described in Table 1 where N is the number of observations, O_i is the i-th observation, S_i is the i-th model simulated value. Results of the calibration analysis will be discussed in section 4.

Table 1
Mode performance indicators [16]

Performance indicator	Description	Formula	
Root Mean Square Error ($RMSE$)	measure of the differences between measured (S) and modelled data	$RMSE = \sqrt{\dfrac{\sum_{i=1}^{N_i}(S_i - O_i)^2}{N_i}}$	(5)
Bias	expresses the difference between an estimator's expectation and the true value	$Bias = \sum_{i=1}^{N}\dfrac{1}{N_i}(S_i - O_i)^2$	(6)
Correlation (R)	a measure of agreement between measured/observed data	*Obtained from excel data analysis package*	
Scatter Index (SI)	the $RMSE$ normalised with the mean value and it provides an indication of the model performance	$SI = \dfrac{\sqrt{\dfrac{1}{N_i}\sum_{i=1}^{N}(S_i - O_i)^2}}{\dfrac{1}{N_i}\sum_{i=1}^{N_i}O_i} \times 100$	(7)

3.9 Model Simulation for Various Scenarios

After calibration, model simulations were run to study the impact of the bridge piers on the hydrodynamics of Gaadhoo Koa atoll pass. In Delft3D, a bridge pier is treated as a porous plate which is defined as a partly transparent structure that have a thickness much smaller than the grid size in the direction perpendicular to the porous plate, that extends into the flow along one of the grid directions while covering some or all layers in the vertical [5]. Partial transparency of the porous plate results in the exchange of mass and momentum across it, generating energy losses. To account for this energy loss, a quadratic energy term is added to the momentum equation as given below.

$$M_\xi = -\frac{C_{loss-u}}{\Delta x} u\sqrt{u^2 + v^2} \tag{8}$$

$$M_\eta = -\frac{C_{loss-v}}{\Delta y} v\sqrt{u^2 + v^2} \tag{9}$$

with c_{loss} the energy loss coefficient or quadratic friction term given by:

$$C_{loss-u} = \frac{NC_{drag}d_{pile}}{2\Delta y}\left(\frac{A_{tot}}{A_{eff}}\right)^2 \tag{10}$$

with:

A_{tot} total cross-sectional area

A_{eff} effective wet cross-sectional area (A_{tot} minus the area blocked by piles: $A_{eff} = A_{tot} - \zeta N d_{pile}$).

C_{drag} the drag coefficient of a pier (pile) (1.0 for a smooth cylindrical pile).

d_{pile} the diameter of a pile.

N the number of piles in the grid cell.

Porous plates are defined inside the grid enclosure and can only be defined at multiples of 45-degree angles with the grid directions. To include porous plates in this work a porous plate file (.ppl) was created which specified the direction of the porous plates normal to the flow, the start and the end node of the grid where the porous plates were located and the vertical layers that the porous plates were extended and finally, the quadratic friction term, C_{loss}. The bridge under this study contains a total of 26 piers and number of piles in these piers and their corresponding diameters obtained from CSET & CDE [3] and the computed friction parameters are listed in Table 2.

Table 2
Bridge pier number, diameters and friction loss parameters

Pier number(s)	Number of piles, N and diameter, d (m)	Friction factor C_{loss-u}	Friction factor C_{loss-v}
1 to 10	$N = 4$, $d = 1.5$	0.298	0.298
11 to 18	$N = 6$, $d = 1.5$	0.576	0.446
19 to 21	$N = 12$, $d = 2.5$ to 2.8	1.185	0.928
22 and 23	$N = 8$, $d = 2.5$ to 2.8	1.185	0.498
24, 25, 26	$N = 4$, $d = 1.5$	0.119	0.119

4. Results and Discussion

4.1 Initial model

The initial model was carried out without the effects of the bridge piers and the results were used for calibration. Figure 5 illustrates the velocity vectors representing tidal flows for both flood and ebb tides at the entrance of Gaadhoo Koa atoll pass. It can be seen that during flood tide the tidal flow is heading towards south and as it approaches the entrance of the channel it shifts south-east eventually flowing easterly as the water moves away from the channel entrance. Conversely, during ebb tide, majority of the tidal flow is oriented north at the entrance point of the channel and as the flow advance further into the atoll, the direction shifts north-west. However, a closer look at the central area in the Figure 5 (right) reveals that part of the tidal flow initially headed north reverses direction at the centre of the region between the two islands and flows back in a south-easterly direction. It can also be observed that the highest flow occurs at the centre of the channel during flood tide with a magnitude ranging from 6 to 10 cm/s. On the other hand, the flow speeds during ebb tide have noticeably lower values ranging from 1 to 4 cm/s. These values indicate that the overall speed of current flow is greater during flood tide when the water is flowing out of the atoll pass towards deeper ocean.
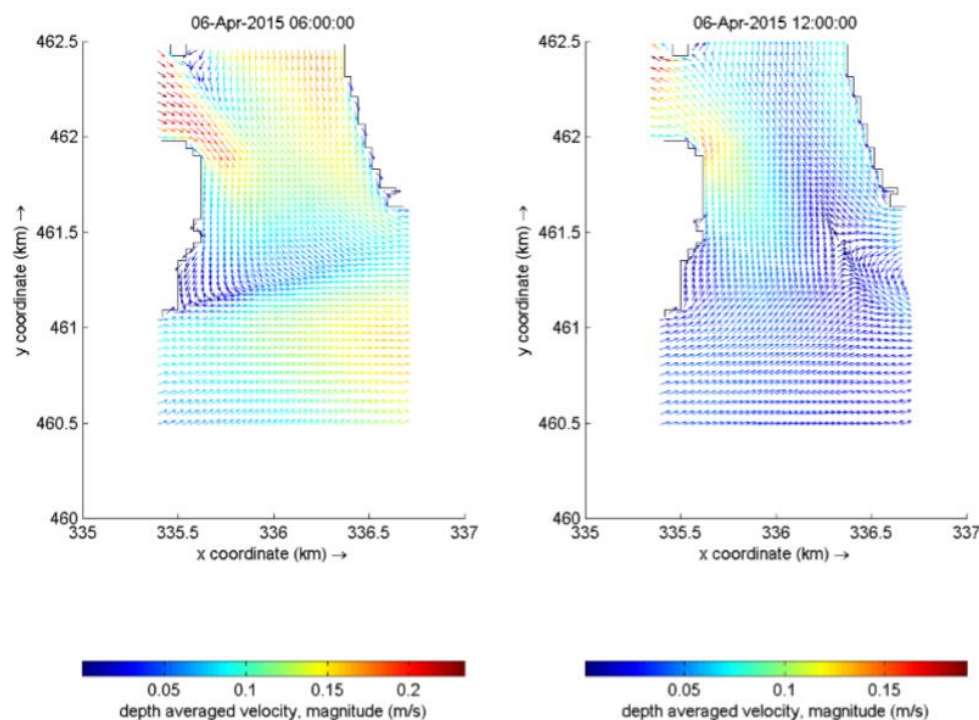
Fig. 5. Flow vectors during flood tide (left) and ebb tide (right)

4.2 Calibration and validation of water level

In order improve the model performance, it was calibrated against the observed water level data from the Hulhulé tide station. Observed data was obtained from 1st April 2015 to 30th April 2015 covering two spring and two neap tide cycles. The calibration parameters considered during calibration were the Manning's friction coefficient, n, which was initially assumed to be 0.02 in both directions and eddy viscosity which was assumed to be $1\ m^2/s$. However, model results for various values of friction coefficient and eddy viscosity revealed no significant improvements in the minor discrepancies between modelled and observed water levels and in some cases these discrepancies

increased. Therefore, it was assumed that the initially assumed values of friction coefficient and eddy viscosity were acceptable in modelling the water level.

The calibrated and observed water levels during neap tide and spring tide cycles are presented in Figure 6 and Figure 7 respectively. It is evident from the figures that the calibrated water levels are in good agreement with the observed water levels. Additionally, it can be observed that over a 24-hour period two low tides and two high tides occurs in both the curves which is a characteristic feature of semi-diurnal tidal patterns. During neap tide water level varied roughly between 0.17 m to -0.2 m resulting in a total tidal range of 0.37 m. On the other hand, during spring tide, water level varied roughly between 0.41 m to -0.44 m resulting in a total tidal range of 0.85 m.
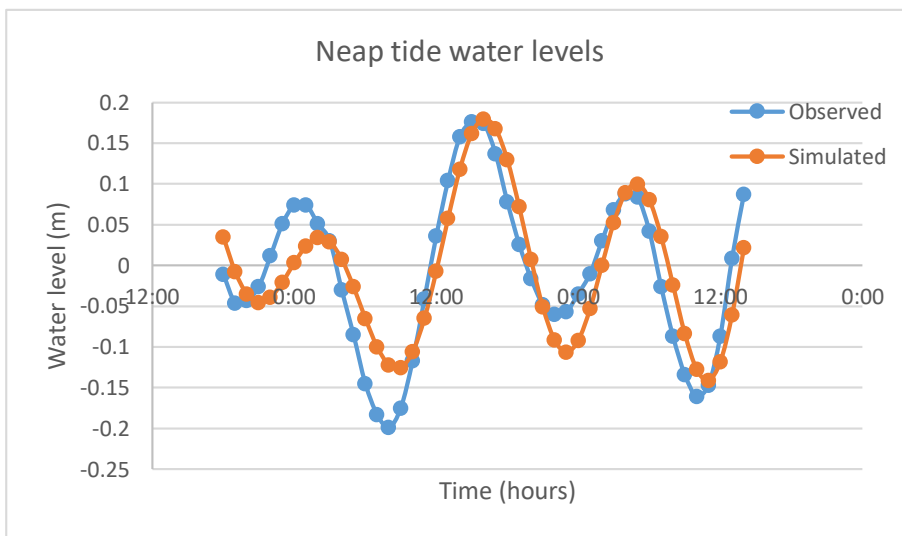
Fig. 6. Neap tide water levels
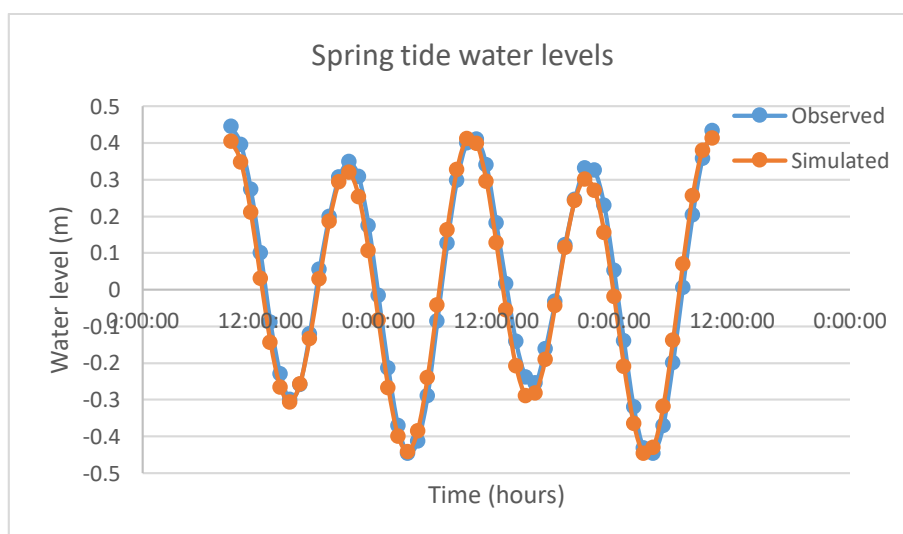
Fig. 7. Spring tide water levels

The standard levels for minimum performance suggested by Williams and Esteves [16] and the computed values for the calibrated model are listed in Table 3. Based on these results, the maximum

mean difference of water level is 0.044 m (4.4%) and 0.045 m (4.5%) during neap tide. Both of these values are less than the standard values of 10% and 15%. Additionally, the calculated bias (0.049) and correlation coefficient (0.985) are also within the acceptable limits.

Furthermore, the scatter index calculated was 1.86% which is less than the standard maximum level of 10%. Therefore, it can be concluded that the calibrated model accurately simulates both spring and neap tidal levels.

Table 3
Results of statistical analysis for model performance

Performance indicator	Standards for minimum level of performance	Calculated values for calibrated water level
RMSE spring tide	10% of the measured level	4.4
RMSE neap tide	15% of the measured level	4.5
Bias	<0.10	0.049
R	>0.95	0.985
SI	<10%	1.86 %

4.3 Simulation of the hydrodynamic impact due to the bridge

Figure 8 shows the magnitude of the residual velocity during flood tide and ebb tide due to the effect of bridge piers. During flood tide, it can be seen clearly that the magnitude of upstream velocity has increased as the flow approaches the bridge and the velocities have decreased in downstream region when the effect of bridge pier is included. However, at the central region of the bridge the downstream velocity increases locally up to a distance of about 200 meters and as the flow proceeds further, it can be observed that the velocity reduces. Further inspections of the impacted area reveal that the influence area for downstream changes in the velocity magnitude extends up to 400 meters laterally from the bridge centre and the majority of these changes are observed on the eastern region of the bridge. The increased upstream and downstream velocities during flood tides in the central region corresponding to the navigational area is similar to the results by Xiao Feng *et al*., [7] showing that at the main navigational area corresponding to the greatest water depth, the upstream velocity increased locally while the downstream velocity decreased. However, the scale of impacted region in this case differs considerably from the results of this research. According to Xiao Feng *et al*., [7], the impacted upstream zone was much smaller compared to the downstream zone while in our case it is the other way around.

Comparing the flood tide observations shows that velocity magnitudes have slightly increased in most of the upstream areas. However, at the vicinity of the bridge, extending from the south western border of Hulhule' island to about a third of bridge length, the velocities seem to have increased in both upstream and downstream direction from the bridge. On the other hand, and the central region of the channel shows reduced velocities in both upstream and downstream direction. The affected downstream distance in these two areas is about twice the length of upstream distance from the bridge. Additionally, at the western end of the bridge, near Male' island, the upstream velocities have reduced while the downstream velocities are slightly higher. Similar to our observations, Xiao Feng *et al*., [7] also showed that during flood and ebb tides, certain portions of the flow possessed an increased velocity region while a certain portion showed reduced velocity. These changes mostly coincide with regions in between piers and regions around piers respectively. Further research needs to be done to analyse the parameters impacting these changes.
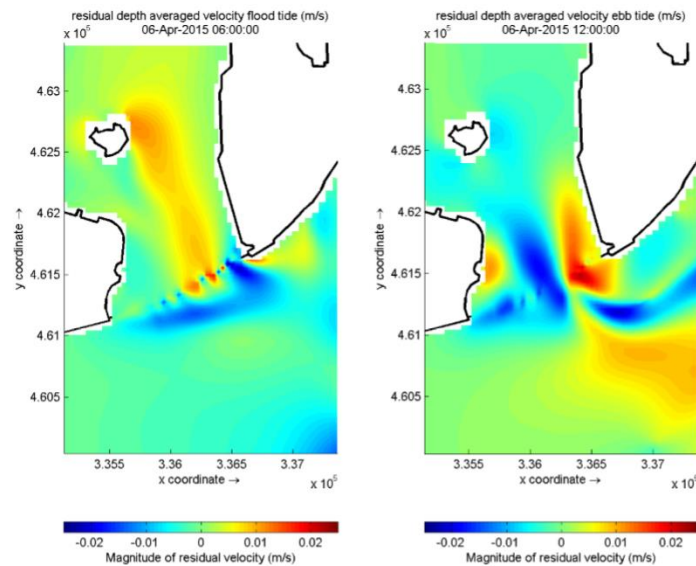
Fig. 8. Magnitude of residual velocity due bridge during flood
(left) and ebb tide (right)

Figure 9 shows the location of observation points selected to compare the current velocities and Figure 10 and Figure 11 shows the corresponding residual velocity profiles from those observation points. Figure 10 shows the residual velocity profile from the observation points located on the northern side of the bridge. A positive value indicates increased velocity due to bridge piers whereas negative value indicates reduced velocities. U1 represents a northern point located in between two piers 100 meters from the major axis of the bridge while U2 represents a northern point located in line with a bridge pier 100 meters from the major axis. U3 and U4 represents a location about 500 meters and 1000 meters respectively from bridge axis. It can observe that U1 shows an increased velocity region for majority of the times since the graph lies slightly above the zero value. On the other hand, U2 shows a reduced velocity region since the graph lies well below the zero value for the majority of the times. Point U3 shows a much less variation in velocities compared to U1 and U2, although it shows a slightly reduced velocity region for the majority of time. Finally, the furthest point from bridge, point U4, shows almost no changes since the graph shows that the residual velocity is almost zero.

Figure 11 shows the residual velocity profile from the observation points on the southern side of the bridge located at the same distances as those in the northern points. As observed with U1, it can be seen that D1 shows an increased velocity region for majority of the times since the graph lies well above the zero value. On the other hand, as observed with U2, D2 also shows a reduced velocity region since the graph lies well below the zero value for the majority of the times. Point D3 shows a slightly increased velocity region for the majority of time. Finally, the furthest point from bridge, point D4, shows slightly increased velocities for the majority of the times, although few instances of reduced residual velocity followed by increased residual velocity can be observed. These observations are consistent with the findings of Hewei *et al*., [4] and Law [14] where decreased velocity regions occurred in front and back areas of the piers while increased velocity regions occurred in areas in between the piers in both directions. In addition, the results Xiao Feng *et al*., [7] also indicted that low flow areas existed at locations around the bridge piers.
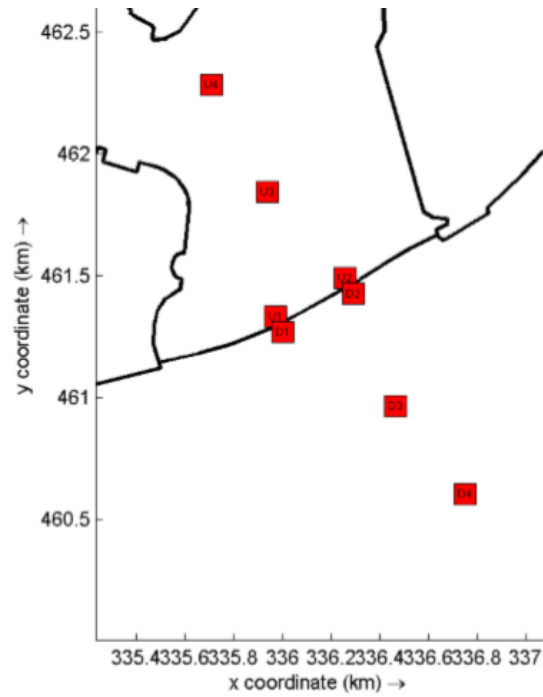
Fig. 9. Locations of the observation points
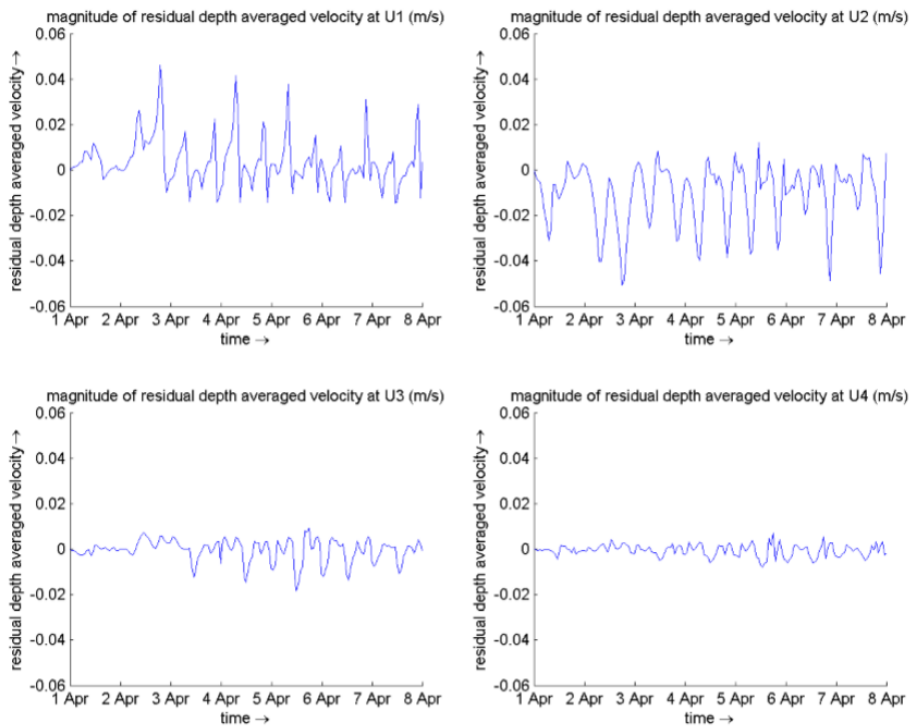
Fig. 10. Magnitude of residual velocities at the northern points
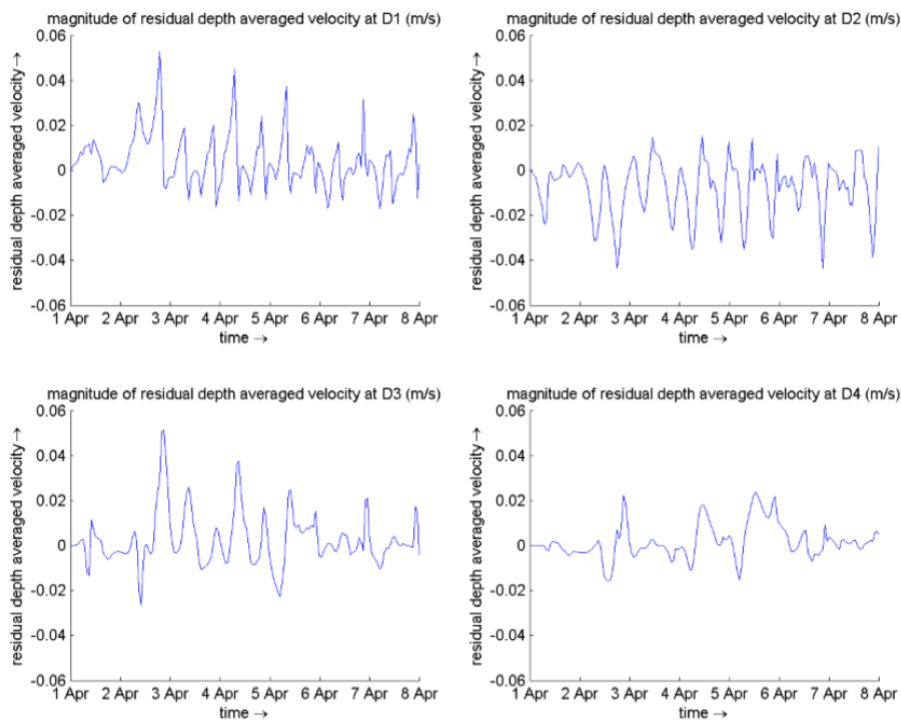
Fig. 11. Magnitude of residual velocities at the southern points

Based on the results from Figures 10 and 11, the majority of velocities reduces in the northern region (peak velocity reduced by 19.2% 500 meters from bridge axis) whereas a rise is observed in the southern region (peak velocity raised by 33% 500 meters from bridge axis). Eventually these variations become almost negligible in the northern region when the distance reaches one kilometre form the bridge axis while in the southern region slightly higher velocities persists one kilometre from the bridge axis. This implies that the degree of velocity variation from the southern region is much greater compared to the northern region and the overall velocity distribution in the northern region from the bridge axis shows a reduced velocity while the southern region shows an increased velocity. However, the velocities changes diminish to none past one kilometre in the norther region while in the southern region slightly higher velocities still persists beyond one kilometre. The observed impacted domain is somewhat consistent with the findings from previous literature. According to Hewei *et al.*, [4], the hydrodynamic simulation of WeiYi Bridge in LiuZhou city, Guangxi province, China, showed that the impacted range was 150 meters on one side of the bridge while it was 1.8 kilometers on the other side. Xiao Feng *et al.*, [7] also showed that the influence domain due to the Sea-Crossing Bridge in Quanzhou Bay was one kilometre in both directions. However, in contrary to the findings of this research, the findings from previous literatures indicates that over all flow velocity reduced in both directions due to the introduction of bridge. This could be due to the fact that the bridge for this research is located in an atoll environment where the hydrodynamical characteristics are thought to be more complicated compared to the bridge sites such as estuaries and rivers being modelled in previous literature. Further studies are needed to accurately identify the model parameters impacting the results by tracking monitoring data and validating the results.

5. Conclusions

In this research, a Delft3D hydrodynamic model was set to study the hydrodynamic processes within the Gaadhoo Koa atoll pass. The calibrated spring and neap tidal levels predicted by the model are in good agreement with the observed water levels. The calibrated model was then used to simulate the effect of a water crossing bridge connecting the two main islands in the region. The simulation results indicated that the bridge piers resulted in a slight change in direction of flow. It was also found that the magnitude of flow velocity reduced around bridge piers and increased in between bridge piers. Furthermore, the overall velocity distribution in the northern region from the bridge axis showed a decreased pattern where peak velocity reduced by 19.2% 500 meters from the bridge while the southern regions showed an increased pattern where peak velocity raised by 33% 500 meters from bridge. Additionally, the observed impacted domain was found to be around one kilometre in northern region and slightly higher than one kilometre in southern region and the degree of velocity variation from the southern region was much greater compared to the northern region. Hence, it can be considered that the introduction of bridge piers has a considerable impact on the hydrodynamic conditions of Gaadhoo Koa channel. However, the model was not calibrated against currents and thus may not have yielded the most accurate current velocities. Further study is required to address these issues.

References

[1] Caldwell, P. C., M. A. Merrifield, and P. R. Thompson. "Sea level measured by tide gauges from global oceans–the Joint Archive for Sea Level holdings (NCEI Accession 0019568), Version 5.5, NOAA National Centers for Environmental Information, Dataset." *Centers Environ. Information, Dataset* 10 (2015): V5V40S7W.

[2] British Oceanographic Data Centre. *GEBCO Digital Atlas: Centenary Edition of the IHO/IOC General Bathymetric Chart of the Oceans*. National Environment Research Council, 2009.

[3] CSET & CDE., Environment impact assessment for the proposed Hulhule-Malé bridge project. China Shipping Environment Technology, China and CDE Consulting, Maldives, 2015.

[4] CUSP., Pre-feasibility report on Scottish Support for Maldives Marine Energy Implementation, Robert Gordon University, Aberdeen, Scotland, 2011.

[5] Deltares, December. "Delft3D-FLOW Simulation of Multi-Dimensional Hydrodynamic Flows and Transport Phenomena Including Sediments, User Manual." (2008).

[6] Egbert, Gary D., and Svetlana Y. Erofeeva. "Efficient inverse modeling of barotropic ocean tides." *Journal of Atmospheric and Oceanic Technology* 19, no. 2 (2002): 183-204.

[7] Guo, Xiao-Feng, Chu-Han Chen, Jun-Jian Tang, and Zhou-Hua Guo. "Numerical simulation study of hydrodynamic Impact of sea-crossing bridge." *Journal of Marine Science and Technology* 24, no. 3 (2016): 493-501.

[8] Indika, K. W., E. M. S. Wijerathne, G. W. A. R. Fernando, and S. S. L. Hettiarachchi. "Sea Level Variability in the East Coast of Male, Maldives." (2017).

[9] Kench, Paul S., Robert W. Brander, Kevin E. Parnell, and Roger F. McLean. "Wave energy gradients across a Maldivian atoll: Implications for island geomorphology." *Geomorphology* 81, no. 1-2 (2006): 1-17.

[10] Li, Pin, Guangxue Li, Lulu Qiao, Xueen Chen, Jinghao Shi, Fei Gao, Nan Wang, and Shuhong Yue. "Modeling the tidal dynamic changes induced by the bridge in Jiaozhou Bay, Qingdao, China." *Continental Shelf Research* 84 (2014): 43-53.

[11] Inaz, Mohamad, Hussein Naeem, Ahmed Jameel, and Mohamad Zuhair. *State of the Environment: Maldives 2004*. Ministry of Environment and Construction, 2004.

[12] *State of the Environment: Maldives 2004*. Ministry of Environment and Construction, 2016.

[13] Pang, Q. X., X. J. Zhuang, Z. H. Huang, and J. C. Sun. "Study on numerical simulation of hydrodynamic conditions influenced by pier in sea." *Journal of Waterway and Harbor* 1 (2008).

[14] Pun, Kwok Leung, and S. Law. "Effects of bridge pier friction on flow reduction in a navigation channel." *Journal of Water Resource and Hydraulic Engineering* 4, no. 4 (2015): 326.

[15] Thurman, Harold V., Alan P. Trujillo, Daniel C. Abel, and Robert McConnell. *Essentials of oceanography*. Upper Saddle River, NJ: Prentice Hall, 1999.

[16] Williams, Jon J., and Luciana S. Esteves. "Guidance on setup, calibration, and validation of hydrodynamic, wave, and sediment models for shelf seas and estuaries." *Advances in Civil Engineering* 2017 (2017).

[17]   Young, I. R. "Seasonal variability of the global ocean wind and wave climate." *International Journal of Climatology: A Journal of the Royal Meteorological Society* 19, no. 9 (1999): 931-950.

[18]   Zhao, Ke, Lulu Qiao, Jinghao Shi, Shufeng He, Guangxue Li, and Ping Yin. "Evolution of sedimentary dynamic environment in the western Jiaozhou Bay, Qingdao, China in the last 30 years." *Estuarine, Coastal and Shelf Science* 163 (2015): 244-253.